Topics in Catalysis (2021) 64:73–83
https://doi.org/10.1007/s11244-020-01295-y

ORIGINAL PAPER

Effects of Ce Doping on the Photocatalytic and Electrochemical Performance of Nickel Hydroxide Nanostructures

C. Martínez-Sánchez[1] · C. Regmi[2] · S. W. Lee[2] · V. Rodríguez-González[3]

Published online: 20 June 2020

Abstract

$Ni(OH)_2$ doped with cerium cations was synthesized by a hydrothermal method and its electrochemical, photoelectrochemical and photocatalytic behavior was determined by the corresponding suitable techniques. $Ni(OH)_2$ films doped with different Ce proportions were evaluated in a KOH support electrolyte solution by cyclic voltammetry. Scan-rate dependent voltammograms displayed pseudo-capacitive behavior while the charge transfer resistance of Ce-doped samples was determined through electrochemical impedance spectroscopy. The calculated charge transfer resistance value was 132 Ω for $Ni(OH)_2$ containing 350 µmoles of Ce. Chronoamperometry under intermittent UV light was employed to measure the photo-response of nanomaterials. The experimental results indicated that the photocurrent of $Ni(OH)_2$ containing 350 µmoles of Ce was ten times greater than that of pure $Ni(OH)_2$. Photocatalytic activity of the powders was demonstrated under UV light irradiation accomplishing 83% of methyl orange degradation after 140 min of reaction with pseudo-first-order kinetics and the calculated degradation rate constant was 0.0125 min^{-1}. The results evidenced the electrochemical, photoelectrochemical and photocatalytic activity of the synthesized materials, which sets them as suitable materials for a wide range of promising photo-based applications.

Keywords $Ni(OH)_2$-Ce · Electrochemical properties · Photoresponse · Photocatalytic · UV-light

1 Introduction

Metal-oxide and hydroxide-based semiconductor materials became popular in several water purification methods such as photocatalysis due to their excellent physical and chemical properties. These materials have also been considered for promising electronic and optoelectronic applications, where MnO_2 [1, 2], RuO_2 [3], NiO [4, 5], $Co(OH)_2$ [6] and $Ni(OH)_2$ [7, 8] are some semiconductor materials that have been reported in the literature. From these examples, $Ni(OH)_2$ is particularly appealing because it is a low-cost material that can be produced by different methods [9–12], has unique electrochemical properties [13] and is environmentally friendly [14]. $Ni(OH)_2$ has had different applications like in the catalytic degradation of nitrite and nitric oxide [15], the photocatalytic degradation of organic compounds under visible light [16], super capacitor electrodes [17] and photoelectrodes [18].

In order to improve the catalytic and electrochemical activity of $Ni(OH)_2$ [14], selective ion doping has been employed because of being one of the most effective methods for this purpose. In this context, lanthanide ions have been reported as ideal dopants in works such as those by K. T. Ranjit et al., who tested the effective lanthanide-oxide-doped-titanium dioxide in the degradation of salicylic and t-cinnamic acids [19], C. Fu et al., who decreased the TiO_2 band gap by incorporating Ce [20] and P. Muthukumaran, who confirmed that Ce-doped NiO nanomaterials exhibited excellent performance in the detection of riboflavin [21]. From these ions, Ce stands out due to the availability of the Ce^{3+}/Ce^{4+} redox pair and the different electronic structures between Ce^{3+} ($4f^15d^0$) and Ce^{4+} ($4f^05d^0$) that can provide

✉ V. Rodríguez-González
vicente.rdz@ipicyt.edu.mx

[1] CONACYT-Centro de Investigación y Desarrollo Tecnológico en Electroquímica, CIDETEQ, 76703 Pedro Escobedo, Querétaro, México

[2] Department of Environmental and Biochemical Engineering, Sun Moon University, Chungnam 31460, Republic of Korea

[3] División de Materiales Avanzados, Instituto Potosino de Investigación Científica y Tecnológica, IPICYT, Camino a la Presa San José 2055, Lomas 4a. sección 78216, San Luis Potosí, S.L.P, México

different optical, catalytic and electron transfer properties [22, 23].

Thus, it is interesting to explore the properties of $Ni(OH)_2$-based materials doped with Ce in order to find out novel applications. This work reports the sustainable synthesis and characterization of $Ni(OH)_2$ doped with Ce. The electrochemical properties of the nanomaterials were determined by cyclic voltammetry and electrochemical impedance. Additionally, the Ce-doped $Ni(OH)_2$ nanomaterials were used as photoelectrodes to evaluate the photo-response under UV-light, which allowed to determine the impact of Ce doping on the photoelectrochemical behavior. Finally, the photocatalytic activity of the Ce- doped $Ni(OH)_2$ nanomaterials was tested in the degradation of the dye methyl orange (MO).

2 Experimental

2.1 Materials

Only analytical-reagent-grade chemicals were acquired. Nickel sulfate (II) hexahydrate and sodium hydroxide were purchased from Sigma-Aldrich; cerium(III) nitrate hexahydrate (Alfa-Aesar, 99.99%), methyl orange (JT Baker), KOH (Sigma-Aldrich) and ultrapure water (supplied by a MilliQ water system) were also used.

2.2 Synthesis of Ni Hydroxide Structures

The synthesis of nickel hydroxide ($Ni(OH)_2$) nanostructures was performed by a hydrothermal method using microwave heating. The precursor solution was prepared by dissolving 7.038 g of nickel sulfate in 70 mL of 7.0 M NaOH; the solution was kept under vigorous stirring for 1 h at 700 rpm.

To obtain $Ni(OH)_2$ doped with different Ce proportions, appropriate amounts of cerium nitrate were dissolved in 30 mL of water to obtain 214, 350 and 710 µmoles of cerium in the samples. The solutions were added dropwise to the precursor solution ($Ni(OH)_2$) under constant stirring, and finally, they were sonicated for 5 min to ensure complete dissociation. The mixtures were transferred to a Teflon reactor, put into a microwave synthesizer (Eyela MWO-1000 Wave Magic) and heated at 120 °C for 4 h. After this time, pale green precipitates were obtained and washed with distilled water and ethanol several times. The final material was recovered using a rotary evaporator at 80 °C. Finally, the powders were dried at 80 °C for 12 h in an oven and then treated thermally at 200 °C for 2 h in order to remove precursor remnants. The obtained products were labeled as $Ni(OH)_2$–Ce1, $Ni(OH)_2$–Ce2 and $Ni(OH)_2$–Ce3, which contained 214, 350 and 710 µmoles of Ce, respectively, and compared with pure $Ni(OH)_2$.

2.3 Characterization and Measurements

The as-obtained catalysts were examined with an X-ray diffractometer Rigaku D/Max 2200 h with CuKα irradiation (λ = 1.5406 Å) operated at 40 kV and 40 mA throughout an interval ranging from 10° to 70° (XRD). The Brunauer-Emmett-Teller (BET) specific surface areas of the sample powders were obtained by nitrogen adsorption-desorption, measured on a Nova 3200 gas-sorption system. The pore size distribution was collected by the Barrett-Joyner-Halenda (BJH) method. Ultraviolet-visible (UV-vis) absorption spectra were surveyed using a UV-vis NIR spectrometer (Agilent Cary 5000). Fourier transform infrared spectra (FTIR) were collected by means of a Shimadzu IRTracer-100 spectrophotometer within an interval ranging from 4000 to 400 cm^{-1}. The morphologies of the prepared samples were obtained by scanning electron microscopy (SEM, Helios double beam 600 high resolution) with an operating voltage of 5 kV.

The electrochemical analysis was performed in a conventional three-electrode system using a potentiostat-galvanostat (BioLogic VSP-300) controlled by the EC-Lab software. The working electrode was fabricated from a suspension of 5 mg of photocatalyst sample in 1 mL of deionized water, which was sonicated for 10 min; then, 100 µL were spread on a clean indium tin oxide (ITO) glass substrate (active area of 2.8 cm^2) and allowed to dry at room temperature. A platinum wire and Ag/AgCl 3 M electrode were used as auxiliary and reference electrodes, respectively. 0.1 M KOH was used as supporting electrolyte solution. The cyclic voltammetry measurements were performed throughout a potential interval ranging from 0.0 to 1.0 V, varying the scan rate from 5 to 100 mV s^{-1}. All electrochemical impedance spectroscopy (EIS) experiments were performed between 1 MHz and 0.1 Hz with excitation signal amplitude of 10 mV. The measurements were made under potentiostatic control applying the open circuit potential. The parameters of the equivalent circuits were obtained through the Z-fit program. The photocurrent measurements of the photocatalysts were examined by the chronoamperometry technique both in the dark and under UV light irradiation (λ = 254 nm) applying a constant potential of 0.7 V in the 0.1 M KOH solution and using the same three-electrode cell described above. Data were recorded at intervals of about 50 s by turning on and off the light source.

The photocatalytic activity of Ni hydroxide structures was evaluated through the photodegradation of MO. 0.025 g of each photocatalyst was suspended in 100 mL of dye solution (concentration = 10 mg mL^{-1}). The suspension was stirred in the dark for 60 min in order to reach adsorption-desorption equilibrium. Subsequently, the solution

was irradiated with a UVP mercury pen lamp (λ = 254 nm) positioned in the center of the reactor under continuous stirring. The dye degradation rate was monitored by taking a 3-mL sample every 20 min; the photocatalyst was removed from the rest of the solution by centrifugation at 3800 rpm and then, the supernatant was analyzed by means of a UV-vis NIR spectrophotometer (Agilent Cary 5000) to determine the MO concentration reading at 464 nm.

3 Results and Discussion

3.1 Optical and Morphological Characteristics

The FTIR analysis of the synthesized nanomaterials gave insights into the composition of the surface chemical functional groups of the products. The FTIR spectra of the nanomaterials within the 400–4000 cm^{-1} interval are shown in Fig. 1 and the presence of seven important transmittance bands is observed at 432, 509, 1375, 1427, 1546, 1631 and 3630 cm^{-1}.

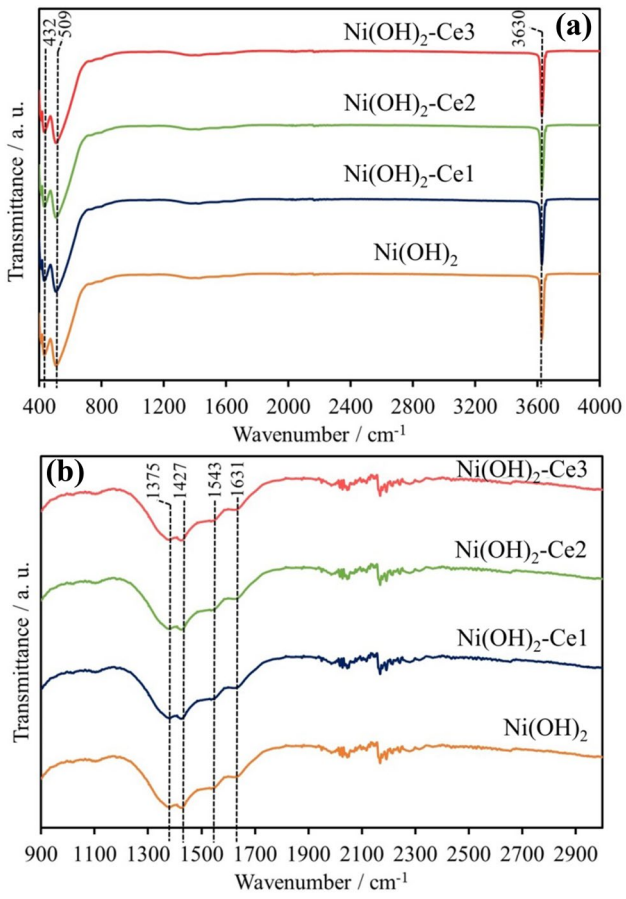

Fig. 1 **a** FTIR spectra of pure and Ce-doped $Ni(OH)_2$ nanomaterials, **b** zoom of the spectra shown in (**a**) between 900 and 3000 cm^{-1}

The narrow band located at 3630 cm^{-1} is attributed to hydroxide O-H stretching of the $Ni(OH)_2$ nanomaterial structure [24] while the band at 1631 cm^{-1} corresponds to the H-O-H bending mode of adsorbed water from the environment [25, 26]. Weak bands located between 1500 − 900 cm^{-1} are due to intercalated carbonate and nitrate groups whereas the weak band near 1427 and 1375 cm^{-1} corresponds to the bending vibration of ionic CO_3^{2-} originated from the reaction of the samples with ambient CO_2 [27]. The bands at 432 and 509 cm^{-1} were assigned to the stretching vibration mode of Ni-O [28]. This result is clear evidence of the presence of nickel hydroxide crystals. The incorporation of Ce cations has no effect on the hydroxide structure.

The XRD patterns of the undoped $Ni(OH)_2$ and other Ce-doped solids treated thermally at 200 °C are shown in Fig. 2. It can be seen that crystalline nickel hydroxide has a hexagonal structure and beta phase (JCPDS 014–0117).

The XRD patterns of the materials with Ce loadings of 214 and 350 μmoles show XRD peaks at around 28.6 from 2 theta. The small peak can be ascribed to the cubic-fluorite-type structure of CeO_2 (JCPDS 00-004-0593). Thus, it is possible to assume that Ce ions can be incorporated into the $Ni(OH)_2$ framework, favoring the formation of NiO and OH groups identified by FTIR. On the other hand, highly dispersed CeO_2 nanoparticles can be formed on the $Ni(OH)_2$ surface, since the peak for cerium oxide is observed. Furthermore, it can be seen that the peaks for the doped samples are less intense and wider than those of $Ni(OH)_2$, which can be possibly due to the incorporation of Ce causing tension between the layers. The peak 001, related to the distance between layers, is clearly an example of the aforementioned [29].

The N_2 adsorption-desorption isotherms for the undoped and $Ni(OH)_2$-Ce2 materials are presented in Fig. 3. The surface area stands from 18 to 57 m^2/g^{-1} for $Ni(OH)_2$ and

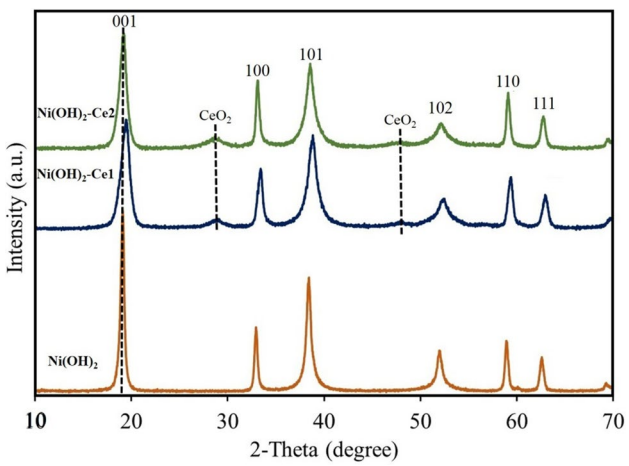

Fig. 2 XRD patterns of Ce-doped $Ni(OH)_2$ nanomaterials

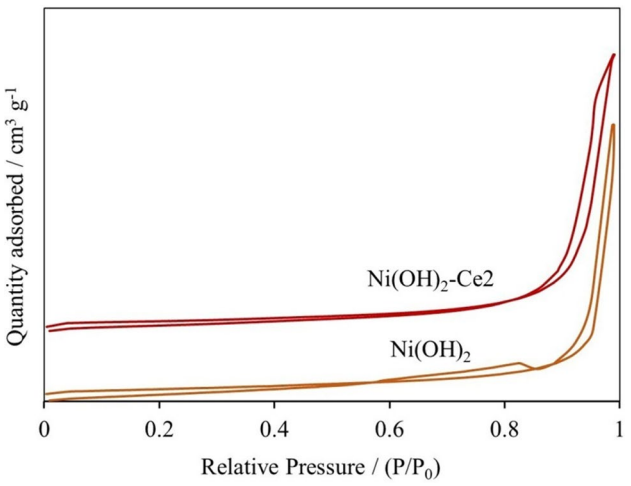

Fig. 3 N_2 adsorption-desorption isotherms of $Ni(OH)_2$ and $Ni(OH)_2$-Ce2 as a representative sample

$Ni(OH)_2$-Ce2 respectively, where the effect of cerium incorporation is the increasing surface area. With 710 moles of cerium, the surface area decreased 2 m^2/g^{-1} approximately (data not shown). The adsorption-desorption isotherms were analogous and dependent on the amount of doped cerium. Thus, the samples are mesoporous materials represented by a type IV isotherm with slight H1 hysteresis loops according to the BDDT classification. The incorporation of cerium promoted the mesoporous texture in the hydroxide, thus facilitating the diffusion of molecules.

The optical absorption property of nanomaterials can significantly estimate their photo-response range. Absorbance spectra were obtained using a reflectance diffuse sphere system. The diffuse absorbance spectra of $Ni(OH)_2$, $Ni(OH)_2$–Ce1, $Ni(OH)_2$–Ce2 and $Ni(OH)_2$–Ce3 are shown in Fig. 4a. For all the samples, two adsorption bands located between 300 and 800 nm are observed, corresponding to the *d–d* transitions of the Ni^{II} cations [30]. It can also be seen that with the addition of Ce, the absorption band centered at around 300 nm is slightly red-shifted, also showing that the absorption intensity of the $Ni(OH)_2$–Ce samples is greater than that of pure $Ni(OH)_2$ in the UV region. This result indicates that the light absorption capacity is increased by doping with Ce; therefore, the samples are suitable for the absorption of UV photons. The absorption edges of $Ni(OH)_2$ appear at 475 nm while $Ni(OH)_2$–Ce1 absorbed at 500 nm, $Ni(OH)_2$–Ce2 at 550 nm and $Ni(OH)_2$–Ce3 at 515 nm, corresponding to the minimum energy required for photoactivation.

The E_g values obtained for the studied samples were as follows: $Ni(OH)_2$ = 2.61 eV, $Ni(OH)_2$–Ce1 = 2.48 eV, $Ni(OH)_2$–Ce2 = 2.25 eV and $Ni(OH)_2$–Ce3 = 2.4 eV. These results indicate that by increasing the amount of Ce, the E_g is extended to the visible region. The charge transfer between the $Ni(OH)_2$ conduction band and the *4f* orbitals of Ce^{4+} lowers the band gap energy of the samples; the same behavior is observed for $Ni(OH)_2$-Ce1 and $Ni(OH)_2$-Ce2. However, E_g for $Ni(OH)_2$–Ce3 was increased and this effect may be induced by an increase in the electron concentration since a rise above the critical concentration allows partial filling of the conduction band, which in turn blocks the lower energy states and therefore widens the bandwidth [31].

UV-vis spectra of the films formed on the conductive glasses were obtained, Fig. 4b, and the absorption edges are similar to the one obtained from the powder samples. These are 405, 440, 565 and 560 nm for Ni $(OH)_2$, Ni $(OH)_2$–Ce1, Ni $(OH)_2$–Ce2 and Ni $(OH)_2$–Ce3, respectively. The shift in absorption edges may be due to a slight change caused by having the material as a film on the conductive glass. The E_g values calculated for the films were the following: $Ni(OH)_2$ = 3.06 eV, $Ni(OH)_2$–Ce1 = 2.81 eV, $Ni(OH)_2$–Ce2 = 2.19 eV and $Ni(OH)_2$–Ce3 = 2.21 eV.

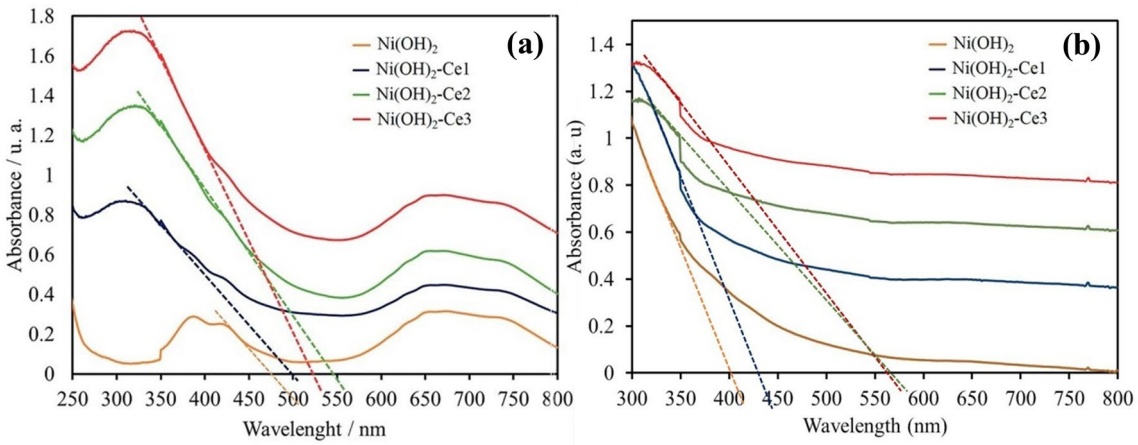

Fig. 4 UV-vis diffuse reflectance spectra of the $Ni(OH)_2$, $Ni(OH)_2$–Ce1, $Ni(OH)_2$–Ce2 and $Ni(OH)_2$–Ce3 nanomaterials (**a**) and films (**b**)

These results indicate that the materials immobilized on the conductive glass displayed a behavior pattern that was similar to that of powder samples.

3.2 Electrochemical Properties

3.2.1 Cyclic Voltammetry

Figure 5 shows the cyclic voltammograms of $Ni(OH)_2$ and the Ce-doped $Ni(OH)_2$ films at different scan rates (100 to 5 mV s^{-1}). The scan was performed using a potential window from 0 to 1.0 V. Anodic and cathodic peaks located at 0.94 and 0.63 V, respectively, were observed for $Ni(OH)_2$ and they can be attributed to the following electrochemical reaction [32, 33]:

$$Ni(OH)_2 + OH^- \leftrightarrow NiOOH + H_2O + e^- \quad (1)$$

Interesting information can be extracted from voltamperograms. Firstly, the shapes of the voltammetry curves of the $Ni(OH)_2$ and Ce-doped $Ni(OH)_2$ films were similar and exhibited characteristics of pseudo-capacitive profiles, very different from the capacitance of the double layer in which the shape is normally close to an almost symmetrical rectangle [33].

Secondly, the calculated difference between the anodic and cathodic peak potential is 310 mV for a scan rate = 100 mV s^{-1}, which is greater than the theoretical value of 59 mV; this result indicates that the redox reaction is quasi-reversible. The I_{pc}/I_{pa} ratio at 5 mV s^{-1} was close to 1, indicating that the system has some degree of reversibility at low scan rates.

Thirdly, it was observed that as the scan rate increased, the current of the anodic and cathodic peaks increased too, which demonstrates the pseudo-capacitance characteristics of the samples while the peak shape is similar to each other. On the other hand, the peak potential was shifted slightly in anodic and cathodic directions, respectively, due to the increase in polarization at high scan rates, resulting in a decrease in capacitance when increasing the scan rate [13].

In addition, the $Ni(OH)_2$-Ce2 film presented more intense redox peaks than all the other samples, indicating that the presence of 350 µmoles of Ce increased the conductivity of the material; therefore, this sample has improved electrochemical activity. This behavior may be related to the fact

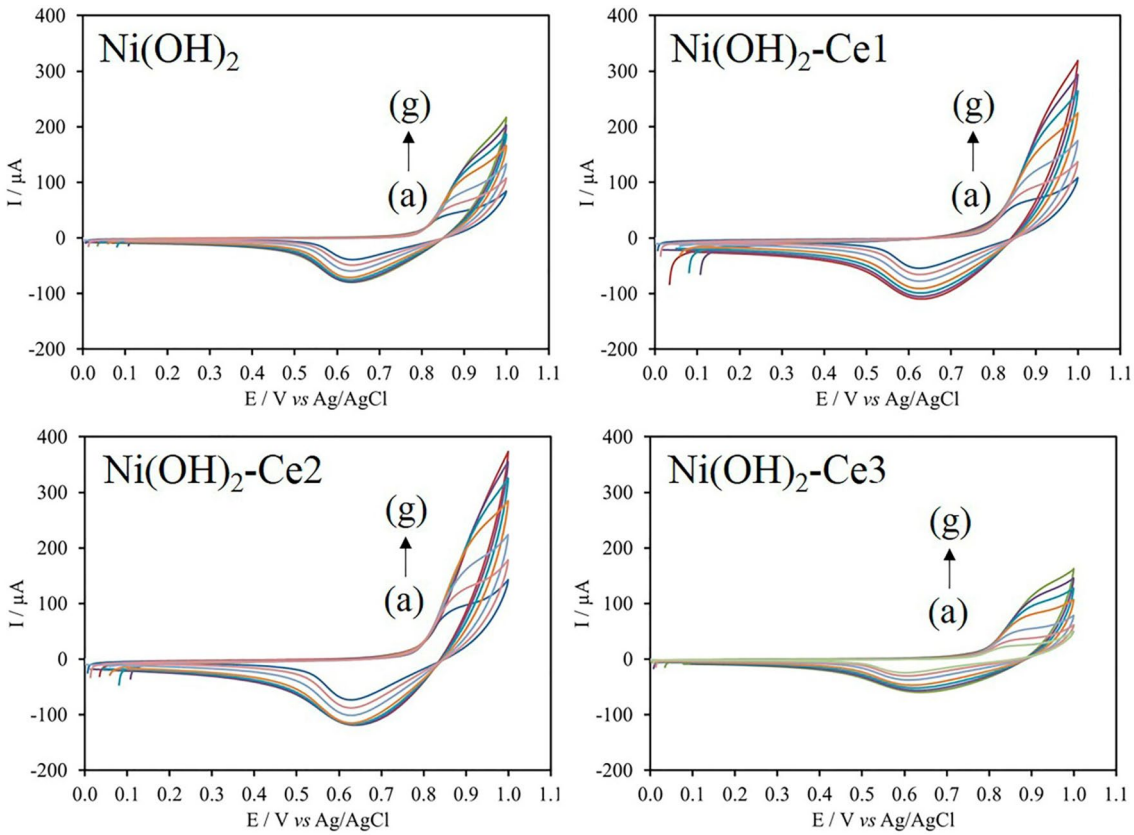

Fig. 5 Cyclic voltammograms of $Ni(OH)_2$, $Ni(OH)_2$–Ce1, $Ni(OH)_2$–Ce2 and $Ni(OH)_2$–Ce3 film electrodes in 0.1 M KOH at different scan rates: **a** 5, **b** 10, **c** 20, **d** 40, **e** 60, **f** 80 and **g** 100 mV s^{-1}

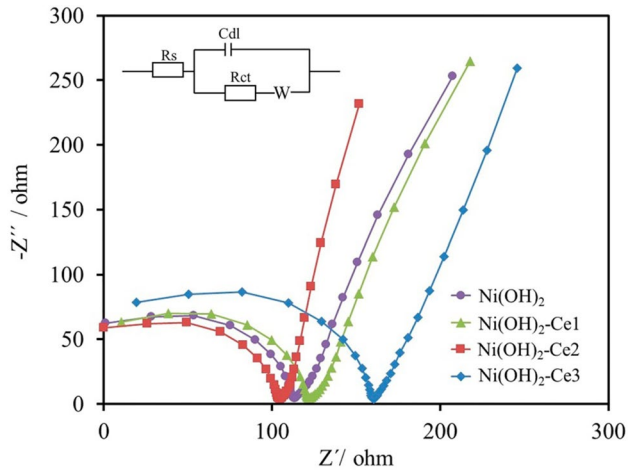

Fig. 6 Nyquist plot obtained from EIS measurements in 0.1 M KOH of $Ni(OH)_2$, $Ni(OH)_2$–Ce1, $Ni(OH)_2$–Ce2 and $Ni(OH)_2$–Ce3 films; frequency range: 10^{-2} to 10^6 Hz. The inset shows the equivalent fitting circuit

that $Ni(OH)_2$–Ce2 has a greater surface area and thus more active sites available for redox reactions to take place.

3.2.2 Electrochemical Impedance Spectroscopy

Electrochemical impedance measurements were made for all the films applying an open circuit potential. The results are shown in Fig. 6, where Z' and Z'' are the real and imaginary parts of the impedance, respectively. For all the films there are two regions that depend on the frequency range, where in high frequency regions a small semicircle and a line in low frequency regions are observed. Generally, the semicircle reflects the impedance of the film electrochemical reaction and the line slope in the low frequency region represents the diffusive resistance (Warburg impedance), resulting from the diffusion of the OH^- ions from the bulk solution to the electrode surface [34]. The more vertical the line, the closer the material is to the ideal capacitor behavior [35]. The shape of the spectra obtained in the present work is similar to those obtained for other $Ni(OH)_2$-based materials [17]. According to Fig. 6, the $Ni(OH)_2$–Ce3 film had a larger arc, which means a greater charge transfer resistance [36]; this fact was verified by calculating the charge transfer resistance (R_{ct}) through the spectra shown in Fig. 6 using the Zfit software. In the inset of Fig. 6, the equivalent circuit used in the impedance spectral adjustment procedure is shown, where R_s and R_{ct} correspond to the resistance of the supporting electrolyte and the charge transfer, respectively; C_{dl} is the double layer capacitance and W is the Warburg impedance. The value of R_s remained practically constant for all the samples between 22.4 and 31.03 Ω while the calculated values of R_{ct} were 141.7, 143.9, 132 and 178.8 Ω for $Ni(OH)_2$, $Ni(OH)_2$–Ce1, $Ni(OH)_2$–Ce2 and $Ni(OH)_2$–Ce3, respectively. Since the $Ni(OH)_2$–Ce2 film had lower R_{ct}, it can be inferred that $Ni(OH)_2$–Ce2 presented a greater reaction surface than the other samples and it was more suitable for charge transfer and OH^- transfer and diffusion into redox active sites. For these reasons, the film increased reactivity and reaction kinetics.

This result is consistent with those observed by cyclic voltammetry. The calculated values of Warburg impedance were 1203, 987.4, 670.4 and 1061 Ω $s^{-0.5}$ for $Ni(OH)_2$, $Ni(OH)_2$–Ce1, $Ni(OH)_2$–Ce2 and $Ni(OH)_2$–Ce3, respectively, meaning that the $Ni(OH)_2$–Ce2 film presents less resistance to the diffusion of OH^- ions within the material pores. Warburg impedance contributes a little to the total impedance, which indicates good contact between the supporting electrolyte ions and the $Ni(OH)_2$–Ce2 material.

3.3 Photoelectrochemical Properties

To further investigate the separation and efficiency of the electrons and photo-generated holes in the $Ni(OH)_2$, $Ni(OH)_2$–Ce1, $Ni(OH)_2$–Ce2 and $Ni(OH)_2$–Ce3 samples, photocurrent measurements were made in a three-electrode system in the dark and under UV light illumination (254 nm), applying a constant potential of 0.7 V; this potential was selected because according to the cyclic voltammograms, there is no interference in the redox reaction at this potential. It is widely known that the diffusion of photoexcited electrons and the collection of photoinduced holes in the electrolyte can generate a photocurrent [37, 38]. The photocurrent-time profiles during five on-off cycles are shown in Fig. 7. The photocurrent response of $Ni(OH)_2$ is minimal (0.09 μA) while the Ce-doped samples reached higher photocurrent levels, suggesting that cerium acts as a charge separator, thus decreasing the recombination. The

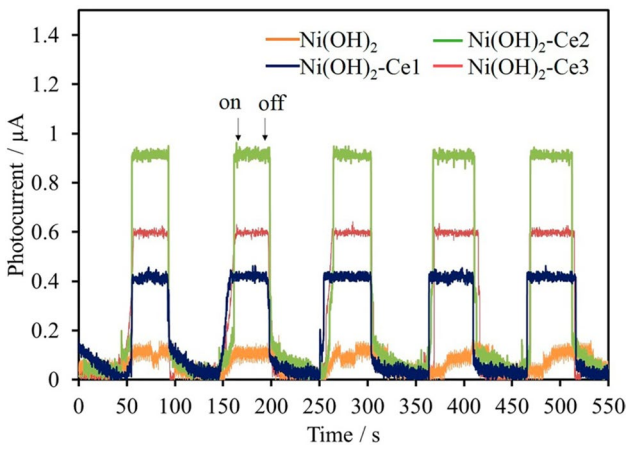

Fig. 7 Photocurrent response of $Ni(OH)_2$, $Ni(OH)_2$–Ce1, $Ni(OH)_2$–Ce2 and $Ni(OH)_2$–Ce3 films in 0.1 M KOH solution under UV light (254 nm)

increasing behavior in the anodic current observed in this work is similar to that of other NiO-metal-based materials [39–42].

The $Ni(OH)_2$-Ce2 film showed higher photocurrent than all the other samples (0.93 μA); as the light was turned on, a rapid current increase was observed, which remained constant until the light was turned off; afterwards, drastic decay occurred. The changes in currents are almost vertical, which indicates that the charge transport rate in the synthesized catalysts was very fast. It is worth mentioning that the photoelectrochemical response shows good stability and reproducibility. This result indicates that the $Ni(OH)_2$-Ce2 sample showed greater separation efficiency and lifetime of photogenerated holes and electrons. Photocurrent values achieved with the $Ni(OH)_2$-Ce2 film are similar to those reported by other authors [40, 43–47]. Particles with higher surface area can increase the contact area with light, which is also consistent with the higher surface area of $Ni(OH)_2$-Ce2.

These results are a precedent for the possible use of $Ni(OH)_2$-Ce2 as photoelectrode in solar cells, UV photosensors or in optoelectronic devices [48–50].

3.4 Photocatalytic Activity

Photodegradation of MO under UV light (254 nm) was performed in order to investigate the photocatalytic activity of the samples. The comparison between the photocatalytic activities of $Ni(OH)_2$ with different proportions of Ce is shown in Fig. 8. Initially, photolysis experiments were performed by irradiating a MO solution in the absence of catalyst. After 140 min of reaction, 31.8% of MO was degraded, where high energy UV irradiation is responsible for the photolysis of MO [51, 52].

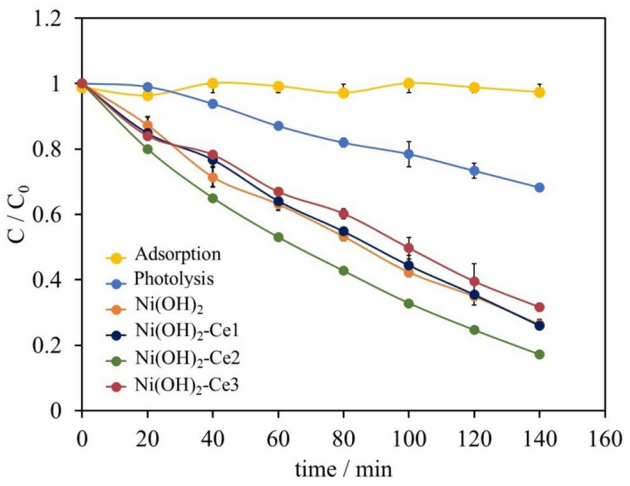

Fig. 8 Degradation curves of 10 mg/L MO using 0.025 g of the synthesized nanomaterials. The degradation experiments were performed under UV light (254 nm)

When degradation occurred using the prepared nanomaterials, it was found that the efficiencies of the photocatalytic degradation of MO were improved to 73.70, 74, 83 and 68.4% for $Ni(OH)_2$, $Ni(OH)_2$–Ce1, $Ni(OH)_2$–Ce2 and $Ni(OH)_2$–Ce3, respectively; which is two times higher than photolysis. It was found that $Ni(OH)_2$–Ce2 had the highest photocatalytic activity, which is in good agreement with what was observed in the photoelectrochemical tests. It is important to emphasize that the possibility of some MO adsorption taking place on the photocatalyst was evaluated, finding that adsorption was negligible.

This result confirms that Ce-doped materials favor the photocatalytic activity possibly because: (1) higher surface area provides more active sites for photocatalytic degradation and (2) the presence of Ce favors the absorption of photons, which can facilitate the generation of electron-hole pairs.

The degradation kinetics of MO was analyzed by a pseudo-first-order kinetic model:

$$kt = -ln(C/C_0) \tag{2}$$

where C and C_0 are the concentrations at time t and time 0, respectively, and k is the degradation rate constant [52]. As shown in Fig. 9a, the plot -ln (C/C_0) vs. time shows good linearity ($R^2 > 0.98$), indicating that photodegradation of MO using the synthesized materials follows pseudo-first-order kinetics. From the slope of this graph, the degradation rate constants (k), Fig. 9b, were obtained, finding that degradation was carried out faster with the $Ni(OH)_2$–Ce2 photocatalyst with $k = 0.0125$ min^{-1}. This value is similar [53–56] and sometimes better than the ones reported in the literature [57–59], having the advantage that in this work, only 0.25 mg mL^{-1} of catalyst were used while others required from 1.0 to 1.5 mg mL^{-1} of catalyst [53, 54, 56]. These results demonstrate the feasibility of using Ce-doped $Ni(OH)_2$ materials for colored wastewater purification.

To understand the behavior of the most active material, SEM and TEM images were obtained for the undoped $Ni(OH)_2$ and $Ni(OH)_2$-Ce2 materials, Fig. 10. Both samples display laminar morphology with different sizes and thickness. The incorporation of cerium to the nickel hydroxide crystals allows the formation of thinner smaller platelets. The doped materials offer high surface area and cerium cations may be available as inhibitors of recombination centers and photoelectrochemical sites. Higher cerium loadings create recombination of surface charged sites for both photoactivity and photoelectrochemical features. The TEM images clearly show that the doping of nickel hydroxide with cerium helped achieve very thin platelets with hexagonal and translucent shapes, which is in contrast with the bare $Ni(OH)_2$ samples.

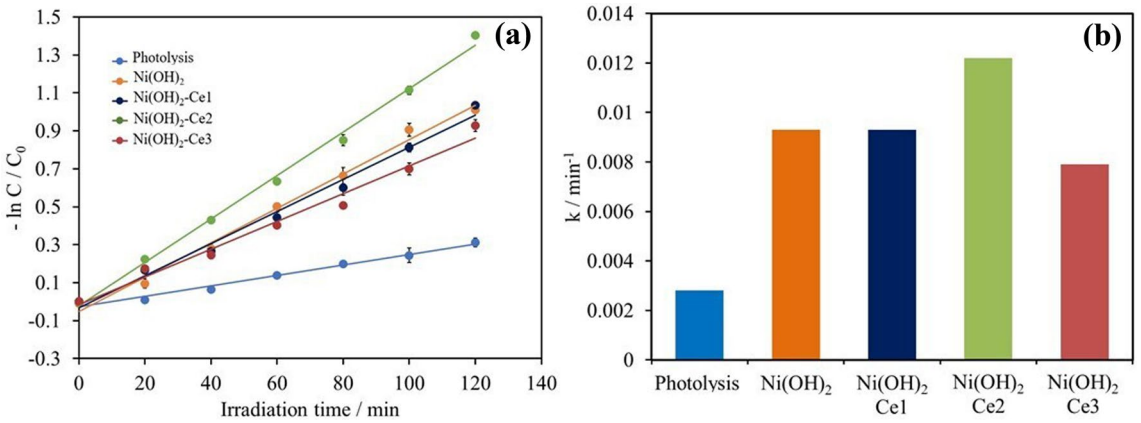

Fig. 9 **a** Graph of -ln (C/C_0) versus irradiation time for the degradation of MO using the synthesized catalysts under UV light (254 nm), **b** degradation rate constants, k, calculated by the pseudo-first-order equation

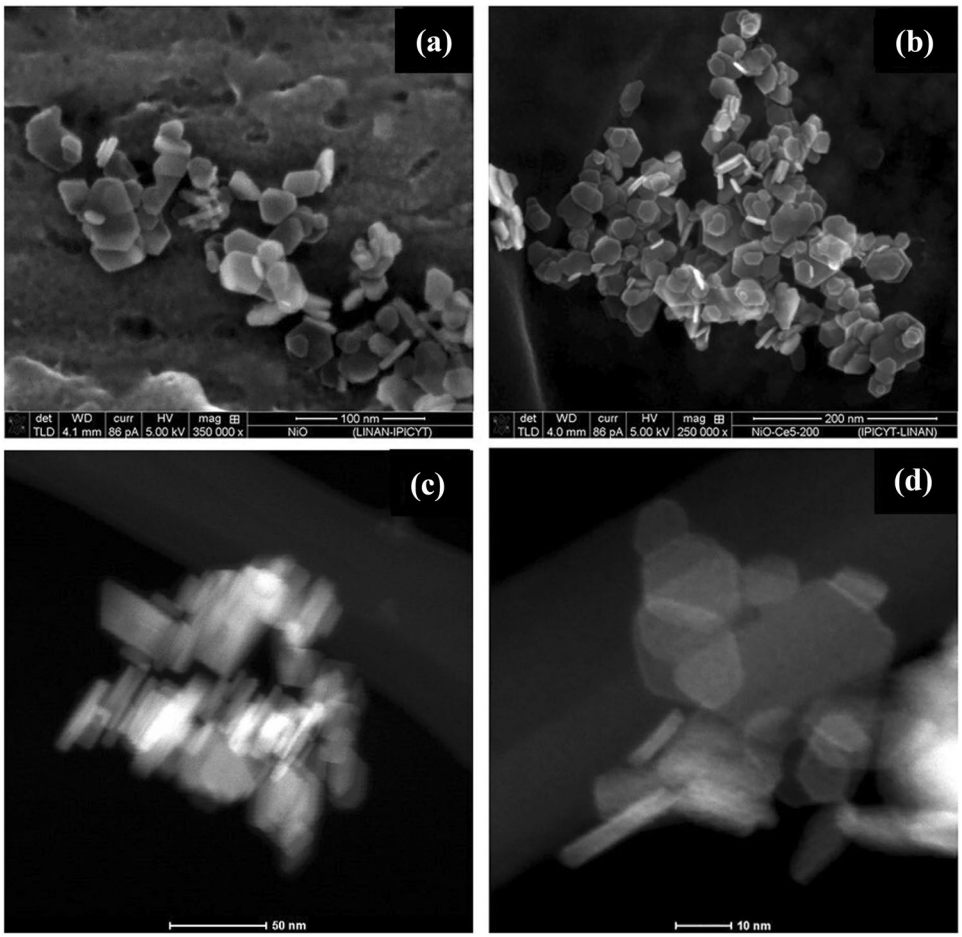

Fig. 10 SEM images of the **a** $Ni(OH)_2$ and **b** $Ni(OH)_2$–Ce2 samples, and HAADF-STEM images of the **c** $Ni(OH)_2$ and **d** $Ni(OH)_2$–Ce2 samples

4 Conclusions

In summary, this work provides new knowledge about photo-based applications of Ce- doped $Ni(OH)_2$ materials. The electrochemical evaluation showed that the synthesized nanomaterials had pseudo-capacitive behavior and the $Ni(OH)_2$–Ce2 sample exhibited lower charge transfer resistance and therefore, it had improved electrochemical activity. The photoelectrochemical analysis under UV light revealed that the performance of $Ni(OH)_2$–Ce2 was ten times greater than that of pure $Ni(OH)_2$ and the

photocurrent rapidly responded to light irradiation. This result indicates that $Ni(OH)_2$–Ce2 can have applications as photoelectrode in solar cells, UV photosensors and optoelectronic devices. The degradation of MO using $Ni(OH)_2$–Ce2 reached 83% after 140 min of irradiation with a UV lamp and the calculated degradation rate constant was 0.0125 min^{-1}; so, this nanomaterial has high potential as a photocatalyst for removing organic contaminants from wastewater. Overall, the photoelectrochemical and photocatalytic evaluation findings set a precedent to develop high photoelectric performance electrodes to be used in the field of photoelectrochemical catalysis.

Acknowledgements C. Martínez-Sánchez appreciates the Postdoctoral scholarship granted by CONACYT. We gratefully acknowledge G. Labrada-Delgado and H. Silva-Pereyra from LINAN-IPICYT for the FESEM and TEM characterizations. V. Rodríguez-González is grateful to KOFTS for the Brain Pool Program No. 152S-2-31424. This research was partially supported by the National Research of Korea (NRF) funded by the Ministry of Education, Science and Technology.

Compliance with Ethical Standards

Conflict of interest The authors declare that they have no conflict of interest.

References

1. Chou S, Wang J, Chew SY, Liu HK, Dou SX (2008) Electrodeposition of MnO_2 nanowires on carbon nanotube paper as free-standing, flexible electrode for supercapacitors. Electrochem Commun 10:1724–1727
2. Wu ZS, Ren W, Wang DW, Li F, Liu B, Cheng HM (2010) High-energy MnO_2 nanowire/graphene and graphene asymmetric electrochemical capacitors. ACS Nano 4:5835–5842. https://doi.org/10.1021/nn101754k
3. Hu CC, Chang KH, Lin MC, Wu YT (2006) Design and tailoring of the nanotubular arrayed architecture of hydrous RuO_2 for next generation supercapacitors. Nano Lett 6:2690–2695. https://doi.org/10.1021/nl061576a
4. Echresh A, Chey CO, Zargar Shoushtari M, Khranovskyy V, Nur O, Willander M (2015) UV photo-detector based on p-NiO thin film/n-ZnO nanorods heterojunction prepared by a simple process. J Alloys Compd 632:165–171. https://doi.org/10.1016/j.jallcom.2015.01.155
5. Sun W, Xiao L, Wu X (2019) Facile synthesis of NiO nanocubes for photocatalysts and supercapacitor electrodes. J Alloys Compd 772:465–471. https://doi.org/10.1016/j.jallcom.2018.09.185
6. Chou S, Wang J, Liu HK, Dou SX (2008) Electrochemical deposition of porous $Co(OH)_2$ nanoflake films on stainless steel mesh for flexible supercapacitors. J Electrochem Soc 155:A926–A929
7. Motahari F, Mozdianfard MR, Soofivand F, Salavati-Niasari M (2014) NiO nanostructures: synthesis, characterization and photocatalyst application in dye wastewater treatment. RSC Adv 4:27654–27660. https://doi.org/10.1039/c4ra02697g
8. Zhang X, Gu A, Wang G, Fang B, Yan Q, Zhu J, Sun T, Ma J, Hoon Hng H (2011) Enhanced electrochemical catalytic activity of new nickel hydroxide nanostructures with (100) facet. CrystEngComm 13:188–192. https://doi.org/10.1039/c003791p
9. Wang X, Luo H, Parkhutik PV, Millan AC, Matveeva E (2003) Studies of the performance of nanostructural multiphase nickel hydroxide. J Power Sources 115:153–160
10. Akinc M, Jongen N, Lemaitre J, Hofmann H (1998) Synthesis of nickel hydroxide powders by urea decomposition. J Eur Ceram Soc 18:1559–1564
11. Jayalakshmi M, Radhika P, Phani Raja K, Mohan Rao M (2007) Solvent and thiourea adsorption/intercalation effects on the solid-state electrochemistry of a-phase nickel hydroxide nanoparticles. J Solid State Electrochem 11:165–172. https://doi.org/10.1007/s10008-005-0081-z
12. Srinivasan V, Weidner JW (1997) An electrochemical route for making porous nickel oxide electrochemical capacitors. J Electrochem Soc 144:L210–L213
13. Li M, Xu S, Zhu Y, Yang P, Wang L, Chu PK (2014) Heterostructured $Ni(OH)_2$-$Co(OH)_2$ composites on 3D ordered Ni-Co nanoparticles fabricated on microchannel plates for advanced miniature supercapacitor. J Alloys Compd 589:364–371. https://doi.org/10.1016/j.jallcom.2013.11.230
14. Zhang Y, Zhao Y, An W, Xing L, Gao Y, Liu J (2017) Heteroelement Y-doped α-$Ni(OH)_2$ nanosheets with excellent pseudocapacitive performance. J Mater Chem A 5:10039–10047. https://doi.org/10.1039/c7ta00963a
15. Adekunle AS, Oyekunle JAO, Oluwafemi OS, Joshua AO, Makinde WO, Ogunfowokan AO, Eleruja MA, Ebenso EE (2014) Comparative catalytic properties of $Ni(OH)_2$ and NiO nanoparticles towards the degradation of nitrite (NO_2^-) and nitric oxide (NO). Int J Electrochem Sci 9:3008–3021
16. Cai X, Cai Y, Liu Y, Deng S, Wang Y, Wang Y, Djerdj I (2014) Photocatalytic degradation properties of $Ni(OH)_2$ nanosheets/ZnO nanorods composites for azo dyes under visible-light irradiation. Ceram Int 40:57–65. https://doi.org/10.1016/j.ceramint.2013.05.103
17. Wang YM, Zhao DD, Zhao YQ, Xu CL, Li HL (2012) Effect of electrodeposition temperature on the electrochemical performance of a $Ni(OH)_2$ electrode. RSC Adv 2:1074–1082. https://doi.org/10.1039/c1ra00613d
18. Mao Y, Yang H, Chen J, Chen J, Tong Y, Wang X (2014) Significant performance enhancement of ZnO photoanodes from $Ni(OH)_2$ electrocatalyst nanosheets overcoating. Nano Energy 6:10–18. https://doi.org/10.1016/j.nanoen.2014.02.008
19. Ranjit KT, Willner I, Bossmann SH, Braun AM (2001) Lanthanide oxide doped titanium dioxide photocatalysts: effective photocatalysts for the enhanced degradation of salicylic acid and t-cinnamic acid. J Catal 204:305–313
20. Fu C, Li T, Qi J, Pan J, Chen S, Cheng C (2010) Theoretical study on the electronic and optical properties of Ce^{3+}-doped TiO_2 photocatalysts. Chem Phys Lett 494:117–122. https://doi.org/10.1016/j.cplett.2010.05.085
21. Muthukumaran P, Chikkili VR, Sumathi C, Slairaj D, Rameshthangam P, Wilson J, Sathish R, Subbiah A (2016) Cerium doped nickel-oxide nanostructures for riboflavin biosensing and antibacterial applications. New J Chem 40:2741–2748. https://doi.org/10.1039/c5nj03539b
22. Liu C, Tang X, Mo C, Qiang Z (2008) Characterization and activity of visible-light-driven TiO_2 photocatalyst codoped with nitrogen and cerium. J Solid State Chem 181:913–919. https://doi.org/10.1016/j.jssc.2008.01.031
23. Regmi C, Maya-Flores E, Lee SW, Rodríguez-González V (2018) Cerium-doped β-$Ni(OH)_2$ hexagon nanosheets: an effective photocatalyst for the degradation of the emerging water pollutant, naproxen. Nanotechnology 29:375603. https://doi.org/10.1088/1361-6528/aace14
24. Iyyappa Rajan P, Judith Vijaya J, Jesudoss SK, Kaviyarasu K, John Kennedy L, Jothiramalingam R, Al-Lohedan HA, Vaali-Mohammed MA (2017) Green-fuel-mediated synthesis of self-assembled

NiO nano-sticks for dual applications—photocatalytic activity on Rose Bengal dye and antimicrobial action on bacterial strains. Mater Res Express 4:08503
25. Sonavane AC, Inamdar AI, Shinde PS, Deshmukh HP, Patil RS, Patil PS (2010) Efficient electrochromic nickel oxide thin films by electrodeposition. J Alloys Compd 489:667–673. https://doi.org/10.1016/j.jallcom.2009.09.146
26. Abd AN, Ali RS, Hussein AA (2016) Fabrication and characterization of nickel heterojunction oxide nanoparticles/silicon. J Multidiscip Eng Sci Stud 2:434–440
27. Mohammad Shiria H, Aghazadeh M (2012) Synthesis, characterization and electrochemical properties of capsule-like NiO nanoparticles. J Electrochem Soc 159:E132–E138
28. Sabouri Z, Akbari A, Hosseini HA, Darroudi M (2018) Facile green synthesis of NiO nanoparticles and investigation of dye degradation and cytotoxicity effects. J Mol Struct 1173:931–936
29. Rodríguez-González V, Marceau E, Che M, Pepe C (2007) Influence of the morphology and impurities of $Ni(OH)_2$ on the synthesis of neutral Ni(II)–amino acid complexes. J Solid State Chem 180:3469–3478
30. Oliver-Tolentino MA, Vázquez-Samperio J, Manzo-Robledo A, González-Huerta RG, Flores-Moreno JL, Ramírez-Rosales D, Guzmán-Vargas A (2014) An approach to understanding the electrocatalytic activity enhancement by superexchange interaction toward OER in alkaline media of Ni-Fe LDH. J Phys Chem C 118:22432–22438. https://doi.org/10.1021/jp506946b
31. Choudhury B, Borah B, Choudhury A (2012) Extending photocatalytic activity of TiO_2 nanoparticles to visible region of illumination by doping of cerium. Photochem Photobiol 88:257–264. https://doi.org/10.1111/j.1751-1097.2011.01064.x
32. Jiang Y, Chen D, Song J, Jiao Z, Ma Q, Zhang H, Cheng L, Zhao B, Chu Y (2013) A facile hydrothermal synthesis of graphene porous NiO nanocomposite and its application in electrochemical capacitors. Electrochim Acta 91:173–178
33. Zhu Z, Ping J, Huang X, Hu J, Chen Q, Ji X, Banks CE (2012) Hexagonal nickel oxide nanoplate-based electrochemical supercapacitor. J Mater Sci 47:503–507. https://doi.org/10.1007/s10853-011-5826-8
34. Wang J (2006) Analytical electrochemisitry: controlled-potential techniques, 3rd edn. Wiley, Hoboken
35. Liu C, Yu Z, Neff D, Zhamu A, Jang BZ (2010) Graphene-based supercapacitor with an ultrahigh energy density. Nano Lett 10:4863–4868. https://doi.org/10.1021/nl102661q
36. Zheng X, Duan S, Liu S, Wei M, Xia F, Tian D, Zhou C (2015) Sensitive and simultaneous method for the determination of naphthol isomers by an amino-functionalized, SBA-15-modified carbon paste electrode. Anal Methods 7:3063–3071. https://doi.org/10.1039/c5ay00027k
37. Tian H, Wan C, Zheng W, Hu X, Qiao L, Wang X (2016) Construction of a ternary hybrid of CdS nanoparticles loaded on mesoporous-TiO2/RGO for the enhancement of photocatalytic activity. RSC Adv 6:84722–84729. https://doi.org/10.1039/c6ra16094h
38. Liu S, Xu YJ (2016) Photo-induced transformation process at gold clusters-semiconductor interface: implications for the complexity of gold clusters-based photocatalysis. Sci Rep 6:1–13. https://doi.org/10.1038/srep22742
39. Long M, Jiang J, Li Y, Cao R, Zhang L, Cai W (2011) Effect of gold nanoparticles on the photocatalytic and photoelectrochemical performance of au modified $BiVO_4$. Nano-Micro Lett 3:171–177. https://doi.org/10.3786/nml.v3i3.p171-177
40. Rebello A, Adeyeye AO (2016) Robust electric-field tunable optoelectrical behavior in Pt-NiO-Pt planar structures. Sci Rep 6:1–8. https://doi.org/10.1038/srep28007
41. Luo Y, Qiao L, Zhang Q, Xu H, Shen Y, Lin Y, Nan C (2018) Tunable photoelectric response in NiO-based heterostructures by various orientations. Appl Phys Lett 112:093301
42. Lv H, Wang C, Li G, Burke R, Krauss TD, Gao Y, Eisenberg R (2017) Semiconductor quantum dot-sensitized rainbow photocathode for effective photoelectrochemical hydrogen generation. PNAS 114:11297–11302
43. Ramasamy P, Kwak D, Lim DH, Ra HS, Lee JS (2016) Solution synthesis of GeS and GeSe nanosheets for high-sensitivity photodetectors. J Mater Chem C 4:479–485. https://doi.org/10.1039/c5tc03667d
44. Yan J, Gu J, Wang X, Fan Y, Zhao Y, Lian J, Xu Y, Song Y, Xu H, Li H (2017) Design of 3D WO_3/h-BN nanocomposites for efficient visible-light-driven photocatalysis. RSC Adv 7:25160–25170. https://doi.org/10.1039/c7ra02929b
45. Fang W, Zhou Y, Dong C, Xiang M, Zhang J (2016) Enhanced photocatalytic activities of vacuum activated TiO_2 catalysts with Ti^{3+} and N co-doped. Catal Today 266:188–196
46. Jiang Z, Wan W, Wei W, Chen K, Li H, Wong PK, Xie J (2017) Gentle way to build reduced titanium dioxide nanodots integrated with graphite-like carbon spheres: From DFT calculation to experimental measurement. Appl Catal B Environ 204:283–295
47. Tian H, Teng F, Xu J, Lou S, Li N, Zhao Y, Chen M (2015) An innovative anion regulation strategy for energy bands of semiconductors: a case from bi 2 o 3 to bi 2 O(OH) 2 so 4. Sci Rep 5:1–9. https://doi.org/10.1038/srep07770
48. Kadam LD, Patil PS (2001) Studies on electrochromic properties of nickel oxide thin films prepared by spray pyrolysis technique. Sol Energy Mater Sol Cells 69:361–369
49. Maciak E, Opilski Z (2007) Transition metal oxides covered Pd film for optical H2 gas detection. Thin Solid Films 515:8351–8355. https://doi.org/10.1016/j.tsf.2007.03.022
50. He J, Lindström H, Hagfeldt A, Lindquist SE (1999) Dye-sensitized nanostructured p-type nickel oxide film as a photocathode for a solar cell. J Phys Chem B 103:8940–8943. https://doi.org/10.1021/jp991681r
51. Fu X, Huang D, Qin Y, Li L, Jiang X, Chen S (2014) Effects of preparation method on the microstructure and photocatalytic performance of ZnSn(OH)6. Appl Catal B Environ 148–149:532–542
52. Wang J, Li H, Meng S, Zhang L, Fu X, Chen S (2017) One-pot hydrothermal synthesis of highly efficient SnO_x/Zn_2SnO_4 composite photocatalyst for the degradation of methyl orange and gaseous benzene. Appl Catal B Environ 200:19–30
53. Znad H, Abbas K, Hena S, Awual MR (2018) Synthesis a novel multilamellar mesoporous TiO_2/ZSM-5 for photo-catalytic degradation of methyl orange dye in aqueous media. J Environ Chem Eng 6:218–227. https://doi.org/10.1016/j.jece.2017.11.077
54. Nguyen CH, Fu CC, Juang RS (2018) Degradation of methylene blue and methyl orange by palladium-doped TiO_2 photocatalysis for water reuse: efficiency and degradation pathways. J Clean Prod 202:413–427. https://doi.org/10.1016/j.jclepro.2018.08.110
55. Saien J, Mesgari Z (2017) Photocatalytic degradation of methyl orange using hematoporphyrin/N-doped TiO_2 nanohybrids under visible light: Kinetics and energy consumption. Appl Organomet Chem 31:1–11. https://doi.org/10.1002/aoc.3755
56. Lv T, Pan L, Liu X, Sun Z (2012) Visible-light photocatalytic degradation of methyl orange by CdS-TiO_2-Au composites synthesized via microwave-assisted reaction. Electrochim Acta 83:216–220. https://doi.org/10.1016/j.electacta.2012.08.018
57. Gupta VK, Saravanan R, Agarwal S, Gracia F, Khan MM, Qin J, Mangalaraja RV (2017) Degradation of azo dyes under different wavelengths of UV light with chitosan-SnO_2 nanocomposites. J Mol Liq 232:423–430. https://doi.org/10.1016/j.molliq.2017.02.095

58. Ökte AN, Yilmaz Ö (2008) Photodecolorization of methyl orange by yttrium incorporated TiO_2 supported ZSM-5. Appl Catal B Environ 85:92–102
59. Arabi M, Baizaee SM, Bahador A, Otaqsara SMT (2018) Rapid, controllable, one-pot and room-temperature aqueous synthesis of ZnO:Cu nanoparticles by pulsed UV laser and its application for photocatalytic degradation of methyl orange. Luminescence 33:475–485. https://doi.org/10.1002/bio.3436